THE ASTROPHYSICAL JOURNAL, 435:722–733, 1994 November 10

THE DUST IN THE HYDROGEN-POOR EJECTA OF ABELL 30

KAZIMIERZ J. BORKOWSKI AND J. PATRICK HARRINGTON
Department of Astronomy, University of Maryland, College Park, MD 20742
WILLIAM P. BLAIR[1]
Department of Physics and Astronomy, Johns Hopkins University, 34th and Charles Streets, Baltimore, MD 21218
AND
JESSE D. BREGMAN
NASA/Ames Research Center, Moffett Field, CA 94035
Received 1994 March 2; accepted 1994 May 11

ABSTRACT

We present new optical and near-infrared images of the hydrogen-poor planetary nebula Abell 30 and produce detailed models that account for the major observed morphological and IR properties. By imaging the nebula in the *K* band, we confirm the presence of hot dust in an expanding equatorial ring of H-poor gas. No emission was detected from the H-poor polar knots, suggesting a dust deficiency there relative to the equatorial ring. The near-IR emission is attributed to small carbonaceous dust grains which are stochastically heated by stellar ultraviolet photons. Using an adaptive version of a matrix method devised by Guhathakurta & Draine (1989) to model stochastic heating, we find that the near-IR spectrum observed by Dinerstein & Lester (1984) requires the presence of dust grains down to ~ 0.0007 μm in radius. This minimum grain radius is in excellent agreement with our calculations of the grain destruction by energetic stellar UV photons: we find that carbon clusters with less than ~ 140 atoms (0.00072 μm in radius) are destroyed by stellar UV photons in ~ 1000 yr, the kinematic age of H-poor ejecta. Modeling of the far-IR dust emission implies that the bulk of the dust mass in A30 must reside at distances several times greater than the distance of the equatorial ring from the central star. This spatial dust distribution is attributed to the interaction of the stellar wind with the inhomogeneous H-poor ejecta. Most of the H-poor gas and dust has been apparently carried outward by the stellar wind, leaving behind dense, H-poor knots with prominent wind-blown tails in the equatorial ring and in the polar knots. This picture is supported by the presence of a stellar wind-blown bubble within the H-rich envelope in our optical images.

Subject headings: dust, extinction — ISM: abundances — planetary nebulae: individual (Abell 30) — stars: mass-loss

1. INTRODUCTION

Abell 30 and Abell 78 are the most prominent members of a class of planetary nebulae (PNe) characterized by H-poor, dusty ejecta. Other members of this group are Abell 58 (V605 Aql), IRAS 18333−2357 (in the globular cluster M22), and IRAS 15154−5258. In these objects the dusty, H-poor material is surrounded by an outer envelope of normal composition (except for IRAS 18333−2357, where ram pressure of the ISM would have stripped off the outer envelope: Borkowski, Harrington, & Tsvetanov 1993a). Apparently a secondary ejection of highly processed material has occurred after the initial expulsion of the hydrogen envelope of the asymptotic giant branch (AGB) progenitor star. The high dust/gas ratio of the secondary ejecta results in strong thermal IR emission which is characteristic of this class.

In fact, the exceptional nature of A30 was signaled by the discovery, first, of strong mid-IR emission (Cohen & Barlow 1974) and, second, of near-IR emission (Cohen et al. 1977). This emission was spatially extended ($\sim 25''$), yet was restricted to a region much smaller than the optical diameter of the nebula (130″). A similar situation was found for A78. Subsequent narrowband imaging (Jacoby 1979) and spectral observations (Hazard et al. 1980; Jacoby & Ford 1983) revealed that these nebulae had, within the outer shell, central knots of gas devoid of hydrogen.

The near-IR observations of Cohen et al. (1977) were puzzling because the implied color temperature of the dust was ~ 1000 K, while the mid-IR colors had indicated that dust in the same location had a temperature of ~ 140 K—typical for PNe. It has been suggested that the high near-IR color temperatures seen in some PNe may arise from temperature fluctuations of very small grains (Phillips, Sanchez Magro, & Martinez Roger 1984), but no quantitative investigation of this effect on the IR emission of A30 has been carried out. Such an analysis is the goal of this paper. (Preliminary findings were reported by Harrington et al. 1993.)

The spatial dust distribution within H-poor PNe is also of interest in view of a recent discovery of wind-blown cometary structures in A30 and A78 (Borkowski et al. 1993b; Clegg et al. 1993). The presence of these cometary structures can be understood by considering the interaction of a stellar wind with the inhomogeneous H-poor ejecta. Strong stellar winds seen in spectra of central stars in both objects (Heap 1986) have broken through the inhomogeneous ejecta, blowing bubbles within the H-rich envelopes and leaving behind dense knots of H-poor gas with wind-blown tails. The stellar wind-blown

[1] Visiting Astronomer, Kitt Peak National Observatory, National Optical Astronomy Observatories, which are operated by the Associated Universities for Research in Astronomy, Inc., under contract with the National Science Foundation.

bubbles can be readily seen in optical images of A30 (Balick 1987) and A78 (Jacoby 1979; Clegg et al. 1993). In the process of this dynamical interaction, a significant fraction of the dusty, H-poor material could have been carried outward to the bubble's edge. Indeed, the presence of the wind-blown cometary structures demonstrates that the H-poor material is continuously being carried outward through a mass-loading process. This is also supported by kinematic evidence for mass-loaded flows in A30 (Harrington 1986) and A78 (Kaler, Feibelman, & Henrichs 1988; Harrington et al. 1994). Manchado, Pottasch, & Mampaso (1988) found H-poor gas close to the bubble's edge in A78, suggesting that an efficient outward transport of H-poor gas has taken place. In view of the high dust content of H-poor ejecta, the thermally emitting dust should be an excellent tracer of these mass-loaded flows. While the near-IR dust emission in A30 is associated with an equatorial ring of expanding H-poor knots (Dinerstein & Lester 1984; this work), the bulk of dust mass appears to be more extended, based on the mid- and far-IR measurements (Cohen & Barlow 1974; Moseley 1980). We investigate the spatial dust distribution in A30 by modeling the IR spectrum of A30, finding that most dust has been carried outward, toward the edge of the wind-blown bubble.

In § 2 we present new optical and K-band imaging of A30 which clarifies the relation of the dust to the H-poor gas. Our optical images clearly show the wind-blown bubble and wind-blown tails. In § 3 we examine in detail the theoretical IR emission from a grain population which includes small grains for which stochastic heating is important. We show that we can fit the observed 1–100 μm fluxes of A30 if the grain-size distribution extends down to a sharp cutoff radius of 0.0007 μm. We also demonstrate that the observed far-IR spectrum requires that the bulk of the dust mass has been carried toward the edge of the wind-blown bubble. In § 4 we examine the evaporation of stochastically heated grains and show that this leads naturally to a minimum size in agreement with that derived from the near-IR spectrum.

2. OBSERVATIONS

Optical CCD/interference filter images of A30 were obtained on 1988 February 23 at the prime focus of the KPNO 4 m Mayall telescope using a TI 800 × 800 pixel CCD. The scale at the 4 m prime focus provided 0.″3 pixel^{-1}, and a full field size of 4′. The conditions were not photometric, as moderate and variable cirrus clouds were present, but the seeing conditions were very stable and very good; star sizes in the images described below indicate effective seeing of 0.″8–0.″9 FWHM.

The filters used were as follows; Hα [λ(cent) = 6565 Å, $\Delta\lambda$ = 30 Å, Trans(peak) = 86%], [O III] [λ(cent) = 5025 Å, $\Delta\lambda$ = 50 Å, Trans(peak) = 80%], and a 6100 Å continuum filter [λ(cent) = 6100 Å, $\Delta\lambda$ = 150 Å, Trans(peak) = 62%]. Exposure times were 1500 s (Hα), 1800 s + 1500 s ([O III]), and 1000 s (6100 Å). Although centered on Hα, the Hα filter width is such that high-velocity emission in [N II] $\lambda\lambda$6548, 6583 could get through the filter (as probably occurs for the knots near the central star; see below). Nonetheless, we will refer to this as the Hα image.

These data were reduced at the telescope using the standard "ccdproc" software, including flat-fielding and bias subtraction. Subsequent data handling has been accomplished using IRAF,[2] where the images have been aligned and the [O III] images were combined. Many of the cosmic rays have been removed from the images using the "imexamine" task in IRAF. The reduced images from Hα and [O III] are shown in Figures 1*a* and 1*b* (Plates 7 and 8).

The Hα image shows a very uniform surface brightness spherical nebula with just a hint of limb brightening at various locations around the edge of the shell. (Balick 1987 classifies its morphology as a round outer halo; we refer to this halo as the H-rich envelope.) Several bright knots are seen in the region within about 10″ of the central star, and a few fainter knots are seen somewhat farther away. Since these inner knots are known to be hydrogen-deficient and to have strong [O III] and [N II] emission (cf. Jacoby & Ford 1983), these knots show up mainly as a result of [N II] $\lambda\lambda$6548, 6583 leaking through the wings of the Hα filter.

The H-rich envelope also appears in the [O III] image, showing slightly more limb brightening than seen in Hα, but with enhancements in basically the same portions of the shell. (The northwest limb may be slightly less enhanced in [O III] compared with other spots.) However, the inner regions show a wealth of detailed structure, with knots and loops extending more than halfway out to the outer shell. We identify these filaments with the boundary of a wind-blown bubble formed as the wind from the central star interacts with the surrounding uniform nebula. It is this material, and in particular the brightest regions directly adjacent to the central star, that are the main concern of this paper.

Figure 2 (Plate 9) shows these inner regions in more detail. The top two panels of this figure have had the 6100 Å continuum image scaled, aligned, and subtracted using IRAF tasks. Two stellar residuals are apparent in these images: the central star and a second star 6″ to the southeast. These stars leave residuals because (*a*) the images were only aligned to the nearest pixel, and (*b*) there are color differences between these two stars over the 5000–6565 Å region. The lower left-hand panel of Figure 2 shows the [O III] data with the contrast stretched to show some of the fainter structures, including the radial striations discussed below.

In addition to these optical images, we have obtained a K-band image of the inner region of A30 using the Lick Observatory Infrared Camera with a 128 × 128 NICMOS II detector on the Lick 3 m telescope (Gilmore, Koo, & Rank 1991). The scale was 0.″36 pixel^{-1}, and the FWHM of a point source after processing was 1.″0. An integration time of 30 s was used for the image, and a 30 s sky frame obtained 60″ away in right ascension was used to subtract the background. The image was then flat-fielded by dividing by a twilight sky frame. Star GD 153, with a K magnitude of 14.29, was used for flux calibration. To examine the diffuse emission from A30, both the central star and its companion lying to the southeast were removed by subtracting the standard star, scaled to the peak of each of the point sources, from the image at the location of the point sources. The reduced K-band image with the central star subtracted was resampled to the 0.″3 pixel size of the optical data and aligned to the optical images using IRAF tasks. This image is shown in the lower right-hand panel of Figure 2 for direct comparison with the optical images. The total K-band flux integrated over the centrally located nebulosity is equal to 6.6 mJy.

Previous studies of A30 have revealed that the morphology of the inner, H-poor knots can be described in terms of an inclined equatorial ring expanding in the northeast-southwest plane. There are also two prominent polar knots located 7″ from the star to north-northeast and south-southeast (we refer to them as the north and south polar knots, respectively). A

[2] IRAF is distributed by the National Optical Astronomy Observatories.

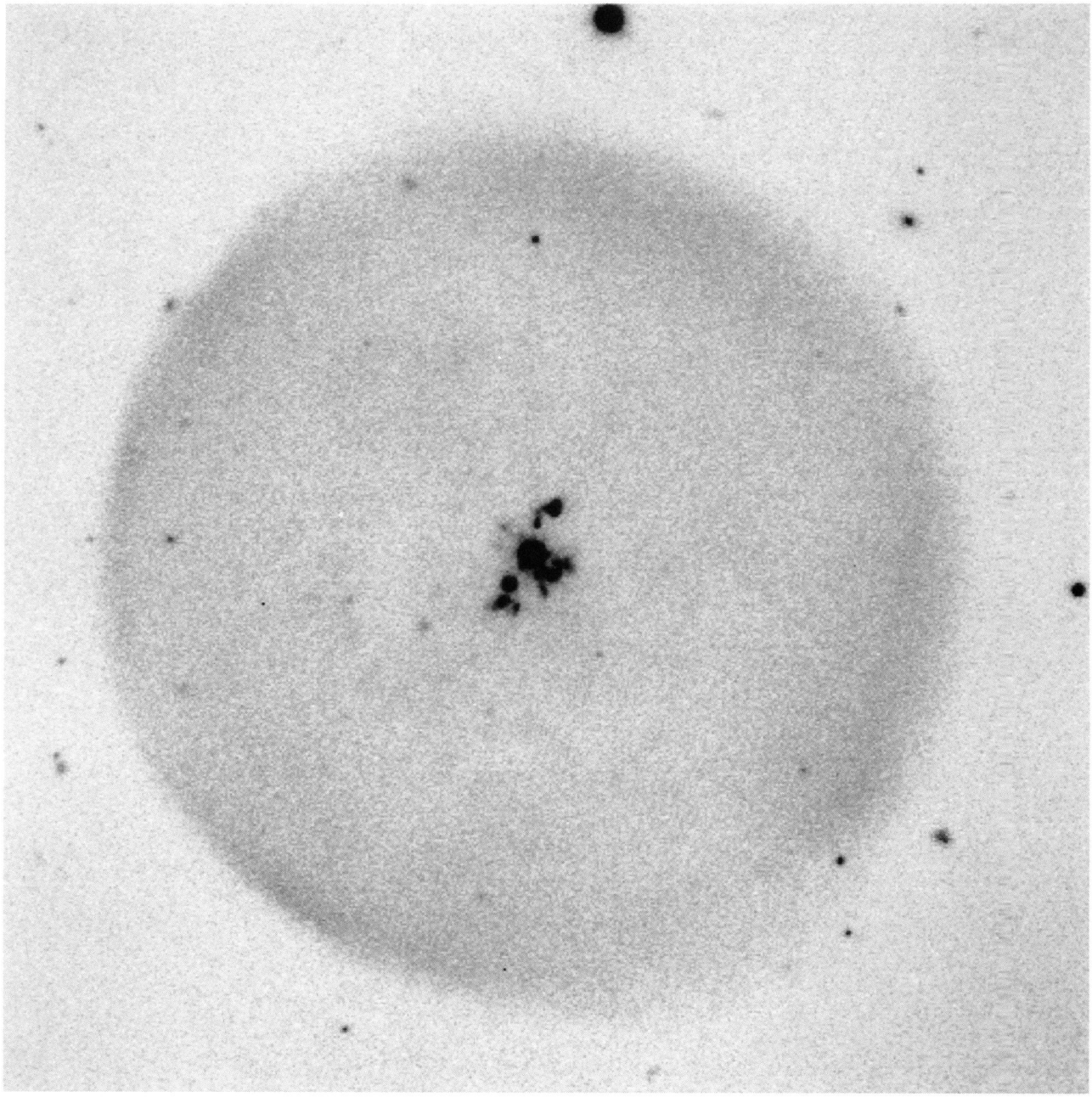

FIG. 1*a*

FIG. 1.—KPNO 4 m prime-focus CCD images of Abell 30. (*a*) Hα. (*b*) [O III] λ5007. The field shown is 2'.5 on a side, with north at the top and east to the left. The central star and a second star 6″ to the southeast are still present in these images. In (*a*) the outer halo is due to Hα, but the inner knots are likely due to [N II] emission that leaks through the filter bandpass (see text). The [O III] image in (*b*) shows much more structure in the inner nebula, and limb brightening of the outer shell is slightly more evident than for Hα.

(BORKOWSKI et al. (see 435, 723)

PLATE 8

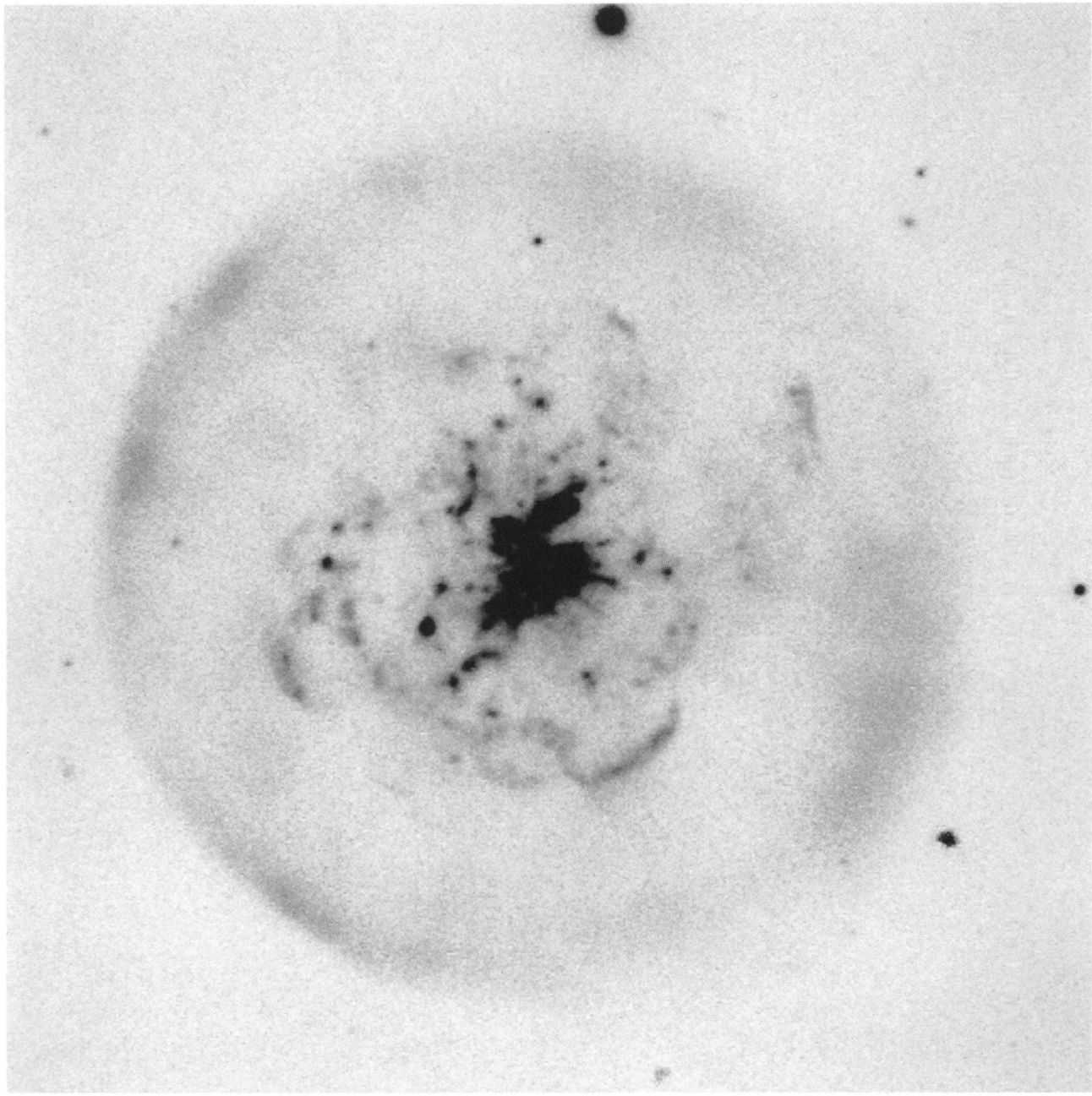

FIG. 1*b*

(BORKOWSKI et al. (see 435, 723)

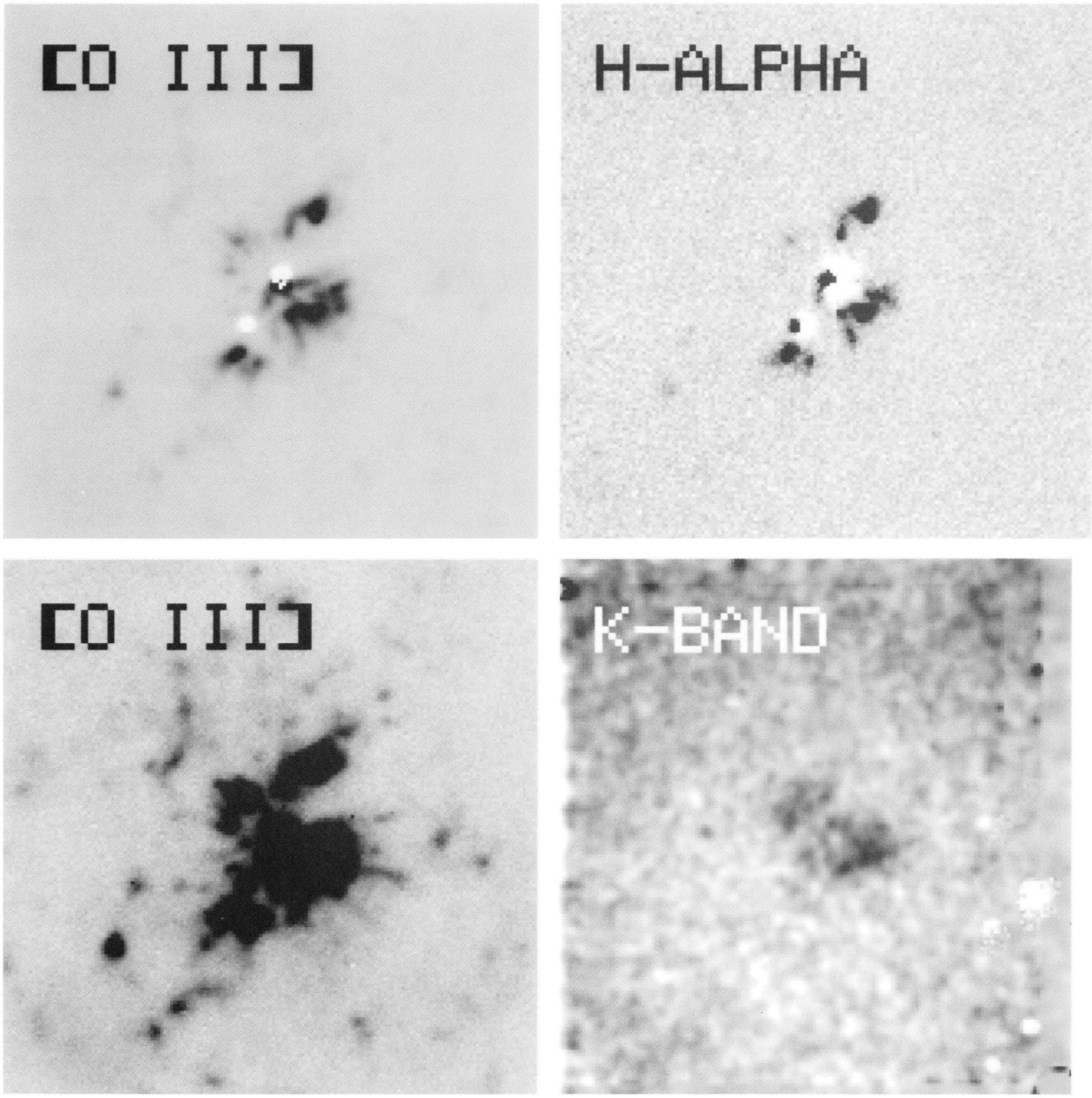

FIG. 2.—Montage of aligned and scaled images of the inner region of A30. The two panels on the left show the [O III] data stretched by different amounts to show more details of the inner structure. The upper right-hand panel shows the Hα image, although the emission seen is mainly from [N II] (see text). The lower right-hand panel shows the background- and central-star–subtracted *K*-band image to the same scale. Each panel is 49″ on a side, with north at the top and east to the left. The optical 6100 Å continuum image has been subtracted from the upper two panels, leaving stellar residuals at the positions of the central star and another star to the southeast.

(BORKOWSKI et al. (see 435, 723)

Hubble Space Telescope (*HST*) [O III] image revealed this equatorial ring to be clumpy, consisting of compact (0".15–0".5) knots with radial tails a couple of arcseconds in length (Borkowski et al. 1993b). We can discern these tails in Figure 2. Our high signal-to-noise [O III] image allows us to trace these tails to significantly larger distances from the central star than were possible with the *HST* data. For example, three prominent, ~5" long tails to the west and northwest are visible in the *HST* image only over a distance not exceeding a couple of arcseconds.

The morphology of the central region of A30 can be understood by considering the interaction of H-poor stellar ejecta with the stellar wind. This wind has been pushing the dusty, H-poor stellar ejecta away from the star. Because of the highly inhomogeneous ejecta distribution, the wind broke through the ejecta and blew a bubble within the H-rich envelope, clearly seen in our optical images. More tenuous ejecta would be strongly accelerated in this process and carried to the outer edge of the bubble. The most dense H-poor condensations could suffer little acceleration and could still move away from the star with their initial ejection velocities. These knots are located within the expanding equatorial ring, well within the wind-blown bubble. In addition, the presence of wind-blown tails behind dense optical emission knots shows that the H-poor material in the knots is being continuously accelerated outward. A fast (in excess of 100 km s^{-1}) outflow detected by Yadoumaru & Tamura (1994) is direct evidence for this acceleration. This accelerated material might eventually mix with the stellar wind, leading to a mass-loaded outflow.

The *K*-band dust emission shows the same northeast-southwest elongation as the lower spatial resolution map made by Dinerstein & Lester (1984). The morphology of our image, with bright knots toward the edges of the extended emission, is suggestive of limb brightening in a ringlike dust distribution the model which Dinerstein & Lester preferred. We conclude that this is the same equatorial ring which is seen in the optical images.

The north and south polar knots of A30 are not seen in our *K*-band image. This result, in agreement with Dinerstein & Lester's observations, suggests a dust deficiency in these knots when compared with the equatorial ring. If the chemical composition of the H-poor gas were the same in the ring and in the polar knots, that would result in higher gas-phase carbon abundances in the polar knots. This is consistent with strong C optical recombination lines seen in the north polar knot (Jacoby & Ford 1983). The origin of the dust deficiency in the polar knots is unknown. It is possible that carbon in the polar knots has not been converted into grains as efficiently as in the equatorial ring. Another possibility is dust destruction in the process of the polar knot formation.

3. THERMAL DUST EMISSION

3.1. *Far-IR Emission and Spatial Distribution of Dust*

IRAS broadband observations of A30 (Pottasch et al. 1984; Leene & Pottasch 1988) confirmed earlier work by Moseley (1980), who found that the bulk of the energy absorbed by dust grains is reradiated in the far-IR. *IRAS* fluxes of 2, 45, 104, and 61 Jy at 12, 25, 60, and 100 μm, respectively, constitute the most fundamental data about dust in A30.

The resolution of *IRAS* was not sufficient to spatially resolve the far-IR emission (Leene & Pottasch 1988; Hawkins & Zuckerman 1991). The FWHM diameter appears to be less than 12" at 12 μm, about 15" and 25" at 25 and 60 μm, respectively, and less than 60" at 100 μm. Moseley (1980) did not resolve the nebula, either, at 70 μm with a 27" beam, but several measurements at 37 μm with a 20" beam indicated a 25" diameter. Cohen & Barlow (1974) also found a spatially extended (25" FWHM) emission in the mid-IR. Therefore, the dust extends farther from the star than the bright central H-poor knots seen in the optical, but it is not associated with the large (2' diameter) hydrogen-rich envelope. Instead, the dust appears to be located within the wind-blown bubble seen in our [O III] image.

A relatively large far-IR–emitting region is also implied by the thermal spectrum. In order to demonstrate this, we modeled thermal emission from two dust distributions: one coinciding with the ring and the other extending to the boundary of the wind-blown bubble seen in optical images. Our models for the (equilibrium) thermal infrared dust emission were constructed using the procedures and computer programs described by Harrington, Monk, & Clegg (1988). The sources for the dielectric constants and other data are given in this reference, except for the amorphous carbon whose optical constants were taken from Rouleau & Martin (1991). Since we know the dust to be carbonaceous (Greenstein 1981), the grain materials considered were graphite and amorphous carbon.

A power-law distribution of grain radii was employed with $N(a) \propto a^{-3.5}$ between the minimum and maximum radii $a_{\rm min} = 0.005$ μm and $a_{\rm max} = 0.25$ μm. This is the standard Mathis, Rumpl, & Nordsieck (MRN) distribution; we discuss below the evidence for the presence of smaller grains and for a possibly different value of the power-law index. Numerical computations were done on a constant-spacing logarithmic grid in grain radius, with 20 grid points for all calculations reported in this work. (We found by numerical experimentation that this number of grid points was sufficient to model infrared spectra accurately.) The stellar radiation field is taken from an LTE model atmosphere by Barstow (1990) (HHECNO101 series: $T_{\rm eff} = 1.2 \times 10^5$ K, $\log g = 6$, and $L = 4000\ L_\odot$), following preliminary non-LTE models of the A78 nucleus by Werner & Koesterke (1992).

Assume first that the dust is confined to the ring seen in our IR image, between 0.02 and 0.04 pc (3".3–6".6) from the central star. The calculated *IRAS* [25 μm]/[60 μm] flux ratio is equal to 0.95 and 1.6 for graphite and amorphous carbon, respectively. The observed *IRAS* flux ratio is equal to 0.43, indicating that the grains are too hot in this model. We must therefore place grains farther from the star in order to obtain agreement with observations. This is consistent with the available information on the spatial extent of the far-IR emission discussed above.

We now consider a simple, uniform dust distribution within the wind-blown bubble with radius 0.2 pc (about 30"), except for an evacuated cavity inside the ring with 0.02 pc radius. With 0.002 $M_\odot$ of amorphous carbon dust, we obtain 2.4, 49, 120, and 72 Jy in the 12, 25, 60, and 100 μm *IRAS* bands, respectively. That compares well with the observed fluxes of 2, 45, 104, and 61 Jy. (A somewhat poorer agreement [0.6, 28, 116, and 50 Jy] is obtained with graphite grains.) The dust spatial extent of 1' in this simple model appears to be larger than implied by observational data discussed above. Apparently the dust distribution in A30 is more concentrated within the wind-blown bubble than in this homogeneous model.

3.2. *Near-IR Emission and Dust Temperature Fluctuations*

The thermal dust models discussed in the previous section produce little emission in the *K* band, failing to account for the

observed flux of 6.6 mJy by orders of magnitude. Near-IR excess emission is not unique to A30; it was noted more than two decades ago in other PNe by Willner, Becklin, & Visvanathan (1972). Phillips et al. (1984) pointed out that this near-IR excess might be caused by small (0.001 μm radius) grains whose temperatures fluctuate in time. Because of their low heat capacity, sufficiently small grains heat up rapidly to high temperatures upon absorption of an energetic photon. The absorbed energy is quickly reradiated at these temperatures, resulting in a rapid grain cooling before the next absorption event. The spectrum of emitted radiation depends on the grain material and the grain size. For example, molecular-sized grains will emit in a variety of emission bands, such as emission features of polycyclic aromatic hydrocarbons (PAHs) seen in many astronomical objects. As the grain size increases, the emitted spectrum becomes more featureless, eventually becoming indistinguishable from that emitted by the bulk material. While PAH emission features are readily seen in numerous PNe, the presence of a hot dust continuum in the near-IR is usually more difficult to establish because of confusion with the numerous emission lines and the free-free continuum from ionized gas. However, recent advances in IR astronomy have made detections of hot dust continua possible in several PNe (Zhang & Kwok 1992; Meixner et al. 1993; Hora et al. 1993).

H-poor PNe are particularly suitable for studying the near-IR dust emission because the free-free continuum and emission lines are very weak in these objects. All near-IR emission can be attributed to the hot dust. From broadband imaging of A30 this emission appears featureless (Dinerstein & Lester 1984), suggesting that we are seeing the hot dust continuum. (In order to confirm this, higher resolution near-IR spectra of A30 would be desirable.)

In order to account for the near-IR hot dust continuum, we extended our thermal dust models described in the previous section to include dust temperature fluctuations. This nontrivial extension is described in detail in Appendix A, together with references to the literature. The method which we use is an adaptive extension of a fast matrix method developed by Guhathakurta & Draine (1989). Following the suggestion by Phillips et al. (1984) about the presence of small dust grains, we extended the MNR distribution down to grain radii of 0.001 μm.

We use bulk optical constants to model emission from small fluctuating dust grains. It is uncertain whether bulk optical constants properly describe the near-IR from small amorphous carbon grains, the grain material implied by the UV extinction seen in the central star of A30 (Greenstein 1981). While the bulk graphite constants definitely cannot be used to model thermal emission from small grains and PAHs (Puget, Léger, & Boulanger 1985), this is caused by the semimetallic nature of graphite. Bulk graphite is a conductor, but the number of electrons per carbon atom in the conduction band is very small. In small graphite grains there are practically no electrons left in the conduction band, leading to the appearance of an energy gap (Puget et al. 1985). In other words, small graphite grains no longer are semimetallic, and their infrared emission cannot be modeled with bulk graphite constants. This argument does not apply to amorphous carbon because this material is not a conductor even for the bulk solid (Robertson 1986). However, if the density of states associated with infrared transitions were low enough, the emission properties of small amorphous carbon grains would be affected by the grain size. In the absence of theoretical and experimental results, we are forced to use bulk optical constants in our calculations. The smooth dust continuum found by Dinerstein & Lester (1984) and the absence of dust emission features suggests that our use of bulk optical constants might not lead to large errors. (However, note that a vibrational quasi-continuum can also produce a smooth spectrum; Allamandola, Tielens, & Barker 1989.)

When temperature fluctuations in a grain population extending to $a_{\rm min} = 0.001$ μm are included in the homogeneous amorphous grain model considered in § 3.1, the 2.2 μm flux is equal to 30 mJy. Of this, about 4 mJy is produced in the ring, at a distance of less than 0.04 pc. This demonstrates that the measured ring flux of 6.6 mJy in the K-band can indeed be accounted for with thermally fluctuating grains. The intensity and spectrum of the near- and mid-IR radiation depends sensitively on the slope of the grain-size distribution and on the size of the smallest grains present. We discuss below what conclusions regarding the grain-size distribution can be drawn from detailed modeling of available IR data for A30.

3.3. *IR Spectrum and Grain-Size Distribution*

Even after choosing the dust dielectric constants, a number of parameters must be specified to construct a model of the thermal IR emission. These include the minimum and maximum grain radii, $a_{\rm min}$ and $a_{\rm max}$, the exponent of the power law of the size distribution, p, and the distribution in space of the dust. Fortunately, these parameters affect different parts of the spectrum, and we thus hope to determine them without too much ambiguity.

It might seem that the spatial distribution of the dust would be of major importance. This would make the modeling difficult in light of the complex morphology of this object. However, while the temperature of the larger dust grains will depend upon their distance from the star, the smallest grains, which are responsible for the emission at wavelengths less than ~ 5 μm, will produce a spectrum which is practically independent of their location. This is because these grains typically are heated to a high temperature by a single photon and then cool down before the next photon is absorbed. Variations in light intensity due to the distance of the dust from the central star will affect the frequency of heating episodes, but the spectrum radiated by the grain during the cooling process will be unchanged.

We find that the one parameter which controls the spectrum in the 1–5 μm range is the minimum grain size, $a_{\rm min}$. In Figure 3 we show the spectrum produced by dust grains with a power-law number distribution, with $p = 3.0$, with grain sizes in the interval $a_{\rm min} < a < 0.25$ μm, for the cases $a_{\rm min} = 5$, 7, 10, 15, and 20 Å. We also show the 7 Å case with temperature fluctuations neglected. The diamonds are the 1.25, 1.65, 2.2, 3.4, 10, and 20 μm fluxes from Figure 3 of Dinerstein & Lester (1984), normalized to our observed flux of 6.6 mJy at 2.2 μm. The dust is assumed to be located in a thin shell at a distance of 0.03 pc from the star. The near-IR spectrum is clearly sensitive to the minimum grain size, and the observations are well fitted by $a_{\rm min} = 7$ Å (0.0007 μm).

With $a_{\rm min}$ determined, we next consider the effect of varying the slope p of the power law, the primary effect of which is to change the ratio of near-IR to far-IR emission through the variation in the ratio of small to large grains. This is illustrated in Figure 4. The dotted, solid, and dashed curves are computed with $p = 2.5$, 3.0, and 3.5, respectively. All three cases are for 0.0007 μm $< a <$ 0.25 μm and a distance of $d = 0.03$ pc. In

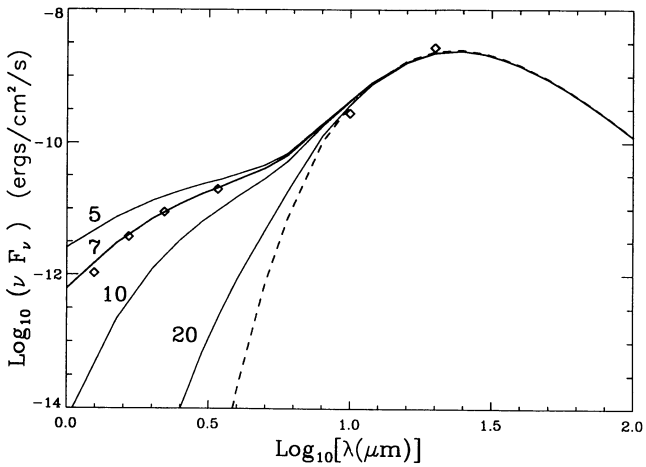

FIG. 3.—Thermal emission from flickering amorphous carbon grains as a function of the grain cutoff radius a_{min}. The curves are labeled with the value of a_{min} in angstroms. The grain population follows a $N(a) \propto a^{-3}$ power law over the range $a_{min} < a < 0.25$ μm. The radiation field is that of a 4000 $L_\odot$ star (see § 3.1) at a distance of 0.03 pc. The dashed curve is the 7 Å case without temperature fluctuations. In this and the following three figures, the diamonds are the observed spectrum of Dinerstein & Lester (1984), scaled to our observed total flux at 2.2 μm. We plot $\log_{10}(\nu F_\nu)$ vs. $\log_{10}\lambda$ so that equal areas represent equal energies.

particular, it is hard to produce enough 20 μm flux with the standard slope of 3.5. We find that a slope of 3.0 is satisfactory, although this choice is not independent of the value of a_{max}. We have insufficient constraints to fix the maximum grain size and have simply used the value assumed in the MRN models.

Finally, we turn to the effects of the distance of the dust on the far-IR spectrum. We can show this clearly by comparing the IR emission of thin shells of constant optical depth (and hence constant total IR luminosity), placed at a series of distances from the star. This is illustrated in Figure 5, for shells at 0.01, 0.02, 0.04, 0.08, and 0.16 pc. We see that the near-IR emission is not affected, but that the peak of the emission in the far-IR shifts to longer wavelengths as the dust becomes cooler with increasing distance from the central star.

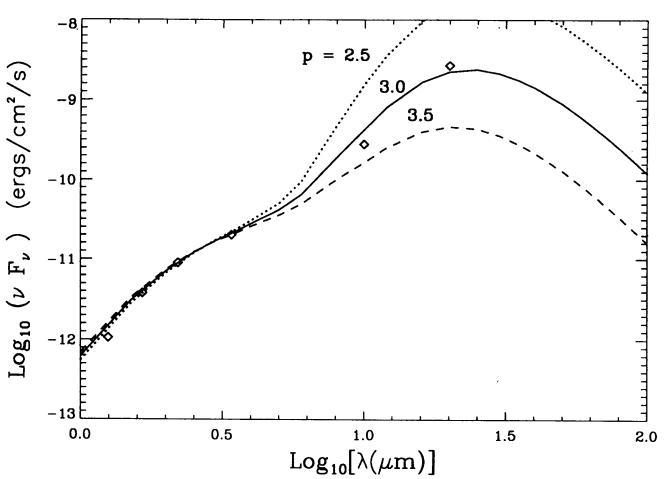

FIG. 4.—Effect of the slope p of a $N(a) \propto a^{-p}$ power-law distribution of grain radii on the thermal infrared emission. The cutoff radii are $a_{min} = 0.0007$ μm and $a_{max} = 0.25$ μm. The grains are located 0.03 pc from the central star. The dotted, solid, and dashed lines correspond to $p = 2.5$, 3.0, and 3.5, respectively.

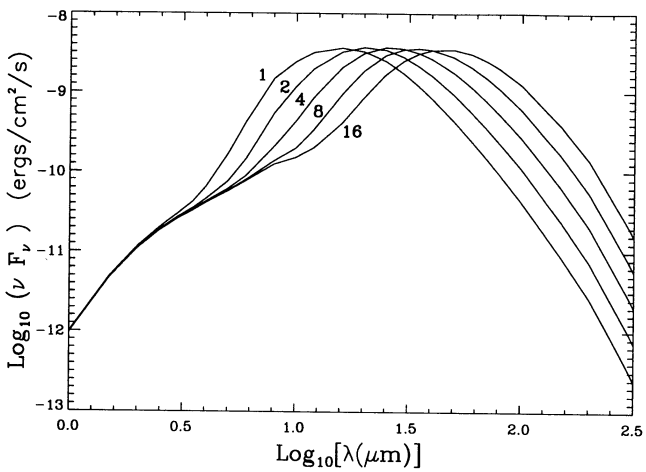

FIG. 5.—Thermal infrared emission from a distribution of grains as a function of distance from the central star. All curves are for $p = 3.0$ and $a_{min} = 7$ Å. The curves correspond to distances of 0.01, 0.02, 0.04, 0.08, and 0.16 pc, respectively.

The real nebula, of course, has dust over a range of distances, and hence cannot be modeled by a single shell. We consider the simplest model capable of representing the data: two shells, one at 0.03 pc (4″.76 at 1.3 kpc) to represent the inner knots, and one at 0.16 pc (25″) to represent the edge of the wind-blown bubble. An additional complication is that the *IRAS* observations include all the flux from the outer shell, while the observations of Dinerstein & Lester (1984) are restricted to the vicinity of the knots. In Figure 6 we present this two-shell model. The solid line is the sum of the flux from both shells and may be compared to the *IRAS* fluxes, while the dashed curve is the contribution of the inner shell only and is to be compared to the Dinerstein & Lester points. We see that a great deal of near-IR emission should also be produced by the outer shell, but this will have a low surface brightness compared to the inner shell, and will be below our current detection limit.

The dust optical depth through the inner shell is $\tau_\lambda = 0.064\, Q(\lambda)$, where $Q(\lambda)$ is the mean absorption efficiency factor

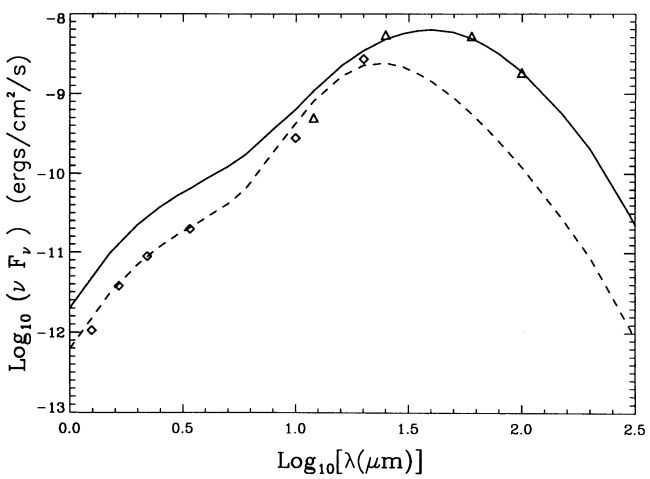

FIG. 6.—Two-shell model for the thermal IR emission of A30. The inner shell is at a distance of 0.03 pc from the central star, and the outer shell at a distance of 0.16 pc. The dashed curve is the flux from the inner shell only, while the solid curve is the total contribution of both shells. The triangles are the *IRAS* fluxes, and the diamonds the normalized fluxes of Dinerstein & Lester (1984).

(Harrington et al. 1988). The IR luminosity of the inner shell is 160 $L_\odot$, and its mass is 3.6×10^{-5} $M_\odot$. The optical depth of the outer shell is 2.2 times that of the inner shell, and the corresponding luminosity and mass are 350 $L_\odot$ and 2.2×10^{-3} $M_\odot$. Thus there appears to be about 60 times more mass in the outer shell than in the inner, which supports the idea that the stellar wind has been at work carrying the dust outward and depositing it at the edge of the bubble. (There could, however, be more dust in the inner zone if it were concentrated in optically thick knot cores.)

4. GRAIN DESTRUCTION BY ENERGETIC PHOTONS

Energetic photons can deposit their energy in a small dust grain, causing a temperature fluctuation which might be large enough for sublimation to occur. In this process, individual atoms escape from the grain when their vibrational energy exceeds their binding energy. Evaporation (sublimation) of small grains by energetic photons is important whenever interstellar dust grains are subjected to a UV or X-ray radiation field. As a result, grains with radii smaller than a critical value are destroyed by evaporation. This should take place in A30, where dust grains are subjected to the hard radiation field of the hot central star. The absence of grains smaller than 0.0007 μm in radius implied by dust modeling in § 3.3 might be caused by their destruction by energetic stellar photons. We demonstrate below that this is indeed plausible.

Evaporation of small grains or large clusters of atoms by energetic photons has been considered previously (Puget et al. 1985; Guhathakurta & Draine 1989; Léger et al. 1989; Voit 1991, 1992). Evaluation of evaporation rates is difficult in general for the cluster sizes of interest—from several tens of atoms to several hundred—because these rates depend on the cluster structure, which might be significantly different from the bulk solid material. Unfortunately, the properties of large carbon clusters relevant for their evaporation are poorly known, which forces us to follow an approximate approach to the evaporation process offered by Guhathakurta & Draine (1989). These authors derived evaporation rates for small graphite grains using bulk graphite properties. We use their evaporation rates in our calculations (eq. [3.13] in Guhathakurta & Draine, with the sticking coefficient set to 0.1), in conjunction with their numerical technique for the dust temperature fluctuations (see Appendix A for the description of our adaptive version of their method). Following Voit (1991), we include evaporative energy losses (energy carried by escaping atoms) in our calculations of temperature fluctuations.

Upon absorption, an energetic photon transfers its energy to a photoelectron, which may escape from a small grain carrying a significant fraction of the original photon energy. Therefore, the efficacy of the energy deposition within the grain depends on the photoelectron escape probability and generally on the nature of the energy loss of energetic electrons within a solid. This topic is discussed in some detail in Appendix B. We present there a simple algorithm to account for photoelectron escape in our calculations of the grain evaporation. This algorithm takes into account the discrete nature of electron energy losses within a solid. For carbonaceous grains the dominant channel for electron energy losses is the collective excitation of valence electrons. The resulting electron oscillations (plasmons) are essentially longitudinal plasma oscillations modified by solid state effects. We demonstrate below that the discrete nature of plasmon excitations is important for the destruction of carbonaceous grains by energetic photons.

We calculated evaporation rates for amorphous carbon grains located at a distance of 0.03 pc from the central star, with radii near the 0.0007 μm cutoff radius determined from our dust model (§ 3.3). A representative example is shown in Figure 7, where the evaporation rate per unit grain enthalpy (atoms yr^{-1} eV^{-1}) is plotted as a function of grain enthalpy for an amorphous carbon grain with 142 atoms (0.00072 μm radius). Absorptions of single photons in the 60–100 eV energy range dominate grain evaporation, with a prominent maximum at 86 eV. This cluster enthalpy range corresponds to temperatures from 2150 to 3200 K. The complex, jagged structure seen in Figure 7 is mostly an artifact caused by the use of a discrete model for the plasmon excitation and the photoelectron escape. Only the break at 54.4 eV is real; the model atmosphere which we use has a large discontinuity at the He^+ ionization edge. Absorption of numerous photons with energies less than 54.4 eV produces a local maximum in the evaporation rate at 50.5 eV. The contribution of these photons to the total evaporation rate is small because evaporation at low temperatures of 2100 K (corresponding to the cluster enthalpy of 50.5 eV) is inefficient. A sharp spike at 65.5 eV is caused by excitation of two plasmons by a photoelectron which subsequently escapes from the cluster. This sharp spike is an artifact; we assumed a delta function for the plasmon shape, while the volume plasmon at 27 eV has in fact a fairly broad width of 15 eV (Raether 1980). If properly accounted for, this broad plasmon width alone would eliminate the jagged structure seen in Figure 7 above 54.5 eV. Following the sharp plasmon spike, the evaporation rate increases with the increasing grain enthalpy because of complete absorptions of photons with energies larger than 65.5 eV. A rapid drop at 75.5 eV is caused by escape of photoelectrons produced by photons with energies larger than 75.5 eV which can overcome the ~ 10 eV potential barrier (the sum of the work function and of the grain potential) after excitation of two plasmons. But there is still a finite probability that photoelectrons produced by these photons will be completely absorbed within the grain. The increasing evaporation rate at energies higher than 75.5 eV is caused by these events. Eventually the evaporation rate decreases because of the shortage of high-energy stellar photons.

The evaporation rate $\dot{N}$ obtained by integrating the curve shown in Figure 7 over the grain enthalpy is equal to 1 atom in 100 yr. The grain lifetime t is the time required to evaporate all of its N atoms. This lifetime is substantially smaller than

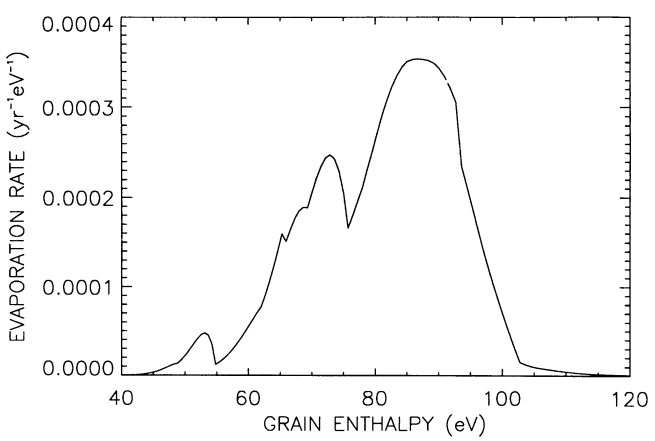

FIG. 7.—Evaporation rate vs. grain enthalpy for an amorphous carbon cluster with 142 atoms (cluster radius $a = 0.00072$ μm) at a distance of 0.03 pc from the central star.

$N/\dot{N}$ = 14,000 yr because of the very steep dependence of the evaporation rate on the cluster size N (Guhathakurta & Draine 1989). From our numerical calculations we find that $\dot{N} \propto N^{-15.2}$ for large carbon clusters of interest in this work. Taking this steep dependence into account, we arrive at the grain lifetime

$$t = 810\left(\frac{N}{140}\right)^{16.2} \text{ yr} . \quad (1)$$

In the example shown in Figure 7 the grain lifetime is comparable to the kinematic age of H-poor ejecta, estimated to be near 1000 yr from high spectral resolution observations (Reay, Atherton, & Taylor 1983; Jacoby & Chu 1989). Because of the steep dependence of the grain evaporation on the cluster size (eq. [1]), the grain-size distribution is expected to have a sharp cutoff at small grain radii. The grain evaporation accelerates so rapidly with decreasing cluster size that grains with less than 120 atoms (0.00068 μm in radius) cannot survive longer than 100 yr, while the lifetime of grains with more than 165 atoms (0.00076 μm) is longer than 10^4 yr. It is gratifying to find that the cutoff radius of 0.0007 μm found from the near-IR thermal dust spectrum coincides with the cutoff expected from our evaporation calculations for clusters with $\sim$140 atoms. While this near-perfect agreement might be fortuitous in view of the many observational and theoretical uncertainties, our calculated cluster cutoff size is only weakly dependent on modeling details because of the steep dependence of the evaporation rate on the cluster size.

5. DISCUSSION AND SUMMARY

Our near-IR, K-band image of A30 revealed a strongly asymmetric dust distribution, in accord with the observations of Dinerstein & Lester (1984). A comparison with our optical images shows that the dust responsible for the near-IR emission is located in an expanding equatorial ring of H-poor gas. The north and south polar knots of A30 are not seen in our K-band image, probably reflecting the dust deficiency in these knots relative to the equatorial ring.

While the dust responsible for the near-IR emission is located in the equatorial ring close to the central star, most of the dust in A30 must reside at significantly larger distances from the star. This has been already hinted by mid- and far-IR observations which marginally resolved the nebula at a diameter almost twice as large as the extent of the equatorial ring. Furthermore, if all dust were located in the equatorial ring, then dust grains would be too hot to explain far-IR observations of A30. We demonstrated this by constructing thermal dust emission models, and found that only $\sim$2% of the total dust mass is located in the equatorial ring, with the bulk of dust mass residing at distances several times greater than the distance of the equatorial ring from the central star.

A large extent of the thermally emitting dust when compared with the optical H-poor ring can be explained by an outward transport of H-poor material from the ring. This is the expected outcome of the interaction of a stellar wind with the inhomogeneous stellar ejecta. Our optical data clearly show signs of this interaction by revealing long (up to 5″) tails of wind-blown material. The presence of dust outside the dense optical knots is thus not surprising. The dust is not expected to extend beyond the outer edge of the bubble blown within the H-rich envelope by the stellar wind, but its distribution within the bubble depends on the poorly understood hydrodynamical processes in the mass-loaded flow.

The emerging picture of the stellar-wind–H-poor gas interaction in A30 apparently involves an inhomogeneous medium where mass loading is important. The abundant dust appears to be an excellent tracer of the H-poor gas which has been carried outward by the stellar wind through the mass-loading process. Because mass-loaded flows are thought to be important in a broader astrophysical context, spatially resolved observations of dust throughout the infrared are warranted in A30 and other H-poor PNe. These observations would also be helpful for understanding the origin of the extremely asymmetric distribution of the H-poor gas seen near the central stars of A30 and A78.

The near-IR dust emission in A30 is produced by stochastic heating of small carbonaceous grains by stellar UV photons. We modeled this process with an adaptive version of a matrix method devised by Guhathakurta & Draine (1989). Using bulk optical constants for amorphous carbon and a power-law distribution of grain sizes, we were able to account for the observed IR spectrum. The calculated near-IR spectrum depends critically on the minimum grain radius $a_{\min}$, which we found to be equal to 0.0007 μm upon comparison with observations. This minimum grain radius is in excellent agreement with our calculations of the grain destruction by stellar UV photons. These calculations took into account both the photoelectron escape and the discrete nature of the energy deposition within the grain by energetic electrons. We found that carbon clusters with less than $\sim$140 atoms (0.00072 μm radius) are destroyed by stellar UV photons in $\sim$1000 yr, the kinematic age of H-poor ejecta.

In order to obtain an agreement with the observed spectral slope throughout the IR, we had to use a relatively flat grain-size distribution, with a power-law index of $p = 3.0$, as opposed to the standard MNR index of $p = 3.5$. This result suggests a relative deficiency of small grains in A30 relative to the interstellar medium. However, further work is necessary in order to confirm this result, because of the uncertainties connected with the poorly known dust distribution and our use of bulk optical constants down to carbon clusters with $\sim$140 atoms. The UV and optical extinction of the central star (Greenstein 1981), caused by the dust within the nebula, is sensitive to the assumed grain-size distribution, and can in principle also be used to constrain this distribution. However, because extinction also depends on the structure of carbonaceous grains, the theoretical analysis of the extinction curve is not straightforward, and will be presented elsewhere.

The presence of small carbon grains with $\sim$140 atoms in the H-poor ejecta of A30 is of considerable interest. In an H-poor environment one can expect "pure" (nonhydrogenated) carbon clusters, in contrast to PAHs seen in most astrophysical objects. On theoretical grounds, the structure of these "pure" carbon clusters is expected to be significantly different from PAHs (Allamandola et al. 1989). For example, one might expect the presence of cagelike structures, exemplified by the buckminsterfullerene (C_{60}) molecule. While C_{60} would be destroyed in A30 by UV photons from the central star, larger cagelike clusters are a distinct possibility. Observations of emission features in the near-IR, such as the C—C vibrational modes near 6 μm, together with the dust continuum, are required to make further progress in identifying carbon clusters responsible for the IR emission. Good-quality IR spectra would also warrant a more detailed modeling effort than is presented in this exploratory work, particularly with regard to the near-IR emission from small carbonaceous grains.

APPENDIX A

NONEQUILIBRIUM THERMAL DUST EMISSION

The cooling time of small dust grains in various astrophysical environments is frequently smaller than the time interval between heating events such as successive photon absorptions. As a result, grain temperatures are not constant but fluctuate with time. Modeling of thermal dust emission must take these fluctuations into account because they strongly affect near- and mid-IR emission. A number of numerical methods have been developed to accomplish this task in the astrophysical context; a recent and powerful matrix method is due to Guhathakurta & Draine (1989). At its basis is a discretization of an integral equation governing the grain temperature fluctuations in temperature space, coupled with an efficient algorithm for the inversion of the resulting matrix. This method (referred to as the GD method) has been used in a number of different astrophysical situations (e.g., Lis & Leung 1991a, b; Siebenmorgen & Krügel 1992; Siebenmorgen, Krügel, & Mathis 1992; Mathis et al. 1992; Natta, Prusti, & Krügel 1993; Wright 1993). Siebenmorgen et al. (1992) discuss the GD method in some detail and compare it with other methods used to account for temperature fluctuations in small dust grains. It is important to note that the GD method should be used with caution because it fails to give accurate results in a number of limiting cases. In particular, it cannot be used for large grains with small temperature fluctuations or to calculate far-infrared emission from small grains.

We present here an adaptive version of the GD method which allows us to calculate thermal emission from dust grains in an automatic fashion, with computational bins chosen by our program. We use an analytical theory of temperature fluctuations in small dust grains presented by Voit (1991) to accomplish this task. We note that Voit (1991) also combined his analytical theory with the GD method to form an integral method to solve for temperature fluctuations. Unlike this integral method, our adaptive program is based on the original formulation by Guhathakurta & Draine, but with computational bins constructed with the help of the analytical theory. In addition to computational advantages, we also find this theory very useful in the interpretation of our numerical results.

We first note that the GD method is not suitable for calculations of temperature fluctuations in big grains whose mean temperatures are nearly equal to equilibrium temperatures. The reason is a fairly wide distribution of grain temperatures around the mean value. When stated in terms of grain enthalpies, one finds that the distribution width is much larger than the average energy delivered to the grain in a single absorption event. In the GD method, one chooses a temperature (or alternatively an enthalpy) range encompassing the region with the nonnegligible grain population for each grain size, and divides it into a number of temperature (enthalpy) bins. Temperature (enthalpy) intervals between the bins must be fine enough to allow for calculations of transition rates between the bins caused by heating events (in our case photon absorptions). It is obvious that these intervals must be significantly smaller than the average energy of the absorbed photon. This requirement demands an excessive number of computational bins for large grains where the enthalpy distribution is much wider than the average photon energy. Therefore, we use an analytical theory to calculate the temperature (enthalpy) grain distribution for large grains. This theory has been presented by Voit (1991) through a formal expansion of equations governing grain temperature fluctuations. In order to illuminate the relevant physical processes and to make connection with a basic theory of stochastic processes, we present below a simple analysis of temperature fluctuations in large grains.

In sufficiently large dust grains multiple photon absorptions are responsible for temperature fluctuations. This suggests that a description in terms of the mean heating rate R_H and a fluctuating component might be suitable in this limit. Accordingly, we assume that the energy H delivered to a grain by stellar photons is given by

$$H(t) = R_H t + \sigma_H \xi(t) , \tag{A1}$$

where the first term on the right-hand side corresponds to the time-averaged (mean) heating and the second term describes the fluctuating component. In the multiphoton absorption limit, this fluctuating component is a Gaussian stochastic process $\sigma_H \xi(t)$ with zero mean and variance $\sigma_H^2 t$. The stochastic process $\xi(t)$ is defined here as a Gaussian process with zero mean and variance t, i.e., a standard Brownian motion. The mean heating rate R_H can be obtained by integrating the energy deposition rate over the photon spectrum,

$$R_H = \int_0^\infty E_{\rm ph} R(E_{\rm ph}, a) dE_{\rm ph} , \tag{A2}$$

where $R(E_{\rm ph}, a)dE_{\rm ph}$ is the absorption rate of photons with energy in the range $(E_{\rm ph}, E_{\rm ph} + dE_{\rm ph})$ by a grain with radius a. (We assume that most photoelectrons do not escape from the grain—certainly a good assumption for large grains of interest here.) Similarly, σ_H is defined by

$$\sigma_H^2 = \int_0^\infty E_{\rm ph}^2 R(E_{\rm ph}, a) dE_{\rm ph} . \tag{A3}$$

Note that σ_H^2/R_H is the mean energy delivered to the grain by those photons which actually heat the grain.

From energy conservation, the grain enthalpy change dE in the time interval dt is given by

$$dE = dH - \mathscr{L}(E)dt , \tag{A4}$$

where $\mathscr{L}(E)$ is the grain cooling rate. Using equation (A1),

$$dE = R_H dt - \mathscr{L}(E)dt + \sigma_H d\xi(t) . \tag{A5}$$

An approximate analytical solution to equation (A5) can be found by expanding the cooling rate $\mathscr{L}$ in a Taylor series around the mean enthalpy $\bar{E}$, and neglecting the quadratic and higher order terms in $E - \bar{E}$. Noting that $R_H = \mathscr{L}(\bar{E})$, we arrive at

$$dE = -\left.\frac{d\mathscr{L}}{dE}\right|_{\bar{E}} (E - \bar{E})dt + \sigma_H \, d\xi(t) \, . \tag{A6}$$

Further, because $\bar{E}$ is independent of time,

$$d(E - \bar{E}) = -\left.\frac{d\mathscr{L}}{dE}\right|_{\bar{E}} (E - \bar{E})dt + \sigma_H \, d\xi(t) \, . \tag{A7}$$

But this is a Langevin equation for $E - \bar{E}$, a linear stochastic differential equation used for modeling the velocity of a particle undergoing Brownian motion. Its solution is known as the Ornstein-Uhlenbeck process (e.g., see Todorovic 1992 for further details and for references to the literature). It is a Gaussian,

$$f(E) = \frac{1}{(2\pi)^{1/2}\sigma} \, e^{(E-\bar{E})^2/2\sigma^2} \, , \tag{A8}$$

with

$$\sigma^2 = \frac{\sigma_H^2}{2d\mathscr{L}/dE|_{\bar{E}}} \, . \tag{A9}$$

Equation (A8) was derived by Voit (1991) through a formal expansion of equations governing grain temperature fluctuations. We also note that Désert, Boulanger, & Shore (1986) had already pointed out the relevance of the Ornstein-Uhlenbeck process for grain temperature fluctuations.

We use equations (A8) and (A9), together with equations (A2) and (A3), to calculate the temperature distribution for large grains. First, we find the equilibrium temperature $\bar{T}$ of a grain with radius a at a particular location within the nebula by equating the grain heating rate at this location with its cooling rate. This equilibrium temperature $\bar{T}$ is then transformed into the mean grain enthalpy $\bar{E}$ using the relation between enthalpy and temperature for graphite given by Guhathakurta & Draine (1989). (This relation is also accurate for amorphous carbon except at very low temperatures of no interest in this work.) Next, we numerically calculate σ from equation (A9). With the enthalpy distribution given by equation (A8) it is now straightforward to calculate the grain thermal emission by dividing the enthalpy range encompassing the Gaussian distribution (e.g., from $\bar{E} - 4\,\sigma$ to $\bar{E} + 4\,\sigma$) into a number of equidistant energy bins (we used 40 bins in our calculations) and weighting the calculated thermal emission from each bin by its population. We used this procedure when the mean (equilibrium) enthalpy was 10 times larger than the mean energy of absorbed photons. In this regime the analytical method is superior to numerical calculations with the GD method. This analytical method might also be useful for those readers not willing to do complete calculations for fluctuating grains. Its implementation is fairly straightforward in a standard equilibrium dust model, with a significant improvement in the mid-infrared region of the spectrum.

As the ratio of the dispersion σ (and the mean energy of absorbed photons) to the mean enthalpy increases, the enthalpy distribution starts to deviate from the Gaussian distribution. While further analytical work is possible here, we found it convenient to use the GD method with an adaptively determined temperature (enthalpy) range. If the mean enthalpy exceeded the larger of the mean energy of absorbed photons and the dispersion σ by a factor of a few (but failed the criterion for a pure Gaussian distribution discussed above), then we chose the temperature range as follows. First, we had to decide on this numerical factor. A factor of 3 is a reasonable choice; we found good agreement by numerical experimentation by setting this factor to 2.5 in our application. Once this criterion was satisfied, we set computational bins in the temperature range corresponding to the enthalpy range $(\bar{E} - 2.5\,\sigma, \bar{E} + 5\,\sigma)$. This enthalpy range, skewed toward higher than average enthalpies, was chosen to encompass grains transiently heated to higher than average energies. Numerical computations were done on a constant-spacing logarithmic grid in temperatures. In order to maintain sufficient accuracy, we used 800 grid points in our calculations. As discussed by Siebenmorgen et al. (1992), a useful check on the numerical accuracy is to compare absorbed and emitted energies which should be equal in accurate calculations.

For smallest grains which failed the above criterion, we set the minimum temperature to 10 K and the maximum temperature to the value where cooling through radiation equals cooling through sublimation, usually around 3000 K in our models. The choice of the minimum temperature is not crucial; all that is required is to choose it low enough so that calculations are not sensitive to its exact value. That will happen when the enthalpy of the lowest computational bin is much smaller than the mean energy of absorbed photons. In addition, the GD method utilizes a fast matrix inversion which fails to produce correct results at low temperatures and long ($> 30\ \mu$m) wavelengths (Siebenmorgen et al. 1992). If this regime is of interest, then one should modify the GD method or use a different one to do the calculation properly. In the present work, however, we are mainly interested in the high-temperature tail of the distribution, i.e., in hot grains. The maximum temperature is thus more important, but again we find that as long as this temperature is high enough, our calculated spectra are insensitive to its exact value. In particular, this is the case at temperatures where cooling through radiation is equal to cooling through sublimation (evaporation). As pointed by Voit (1991), evaporative cooling should be (and is) included in our models, with the help of formulae given by Guhathakurta & Draine (1989). Our calculated spectra are insensitive to this correction to the original GD method.

We found the simple adaptive GD method described above dependable and easy to use in our particular application, unlike the original version. We feel that its parameters can be easily adjusted through numerical experimentation to suit a variety of different situations. The implementation of adaptive features is straightforward, and the use of analytical results eases the interpretation of numerical results.

APPENDIX B

PHOTOELECTRON ESCAPE AND ENERGY DEPOSITION IN SMALL GRAINS BY ENERGETIC PHOTONS

Evaporation of carbon clusters in A30 is caused by large temperature fluctuations occurring upon stellar photon absorptions by these clusters. Consider an absorption of an energetic stellar photon, with energy larger than 50 eV. At these high energies photoelectric absorption is the dominant process (Henke, Gullikson, & Davis 1993), resulting in an excitation of one of the cluster electrons into a high-lying discrete or continuum state. Photoelectron energy may then be transferred into atomic vibrations, raising the cluster temperature to high values at which evaporation might occur. That would correspond to a complete photon absorption. However, this photoelectron may also escape from the cluster, carrying out some of the photon energy. The energy carried by escaping electrons is a small fraction of the absorbed energy for a bulk solid or sufficiently large dust grains. For example, less than 1% of energy absorbed by large interstellar dust grains is transferred to escaping electrons. This fraction is expected to be greater for small grains because of the higher probability of the photoelectron escape. That would result in a smaller amount of energy deposited within the grain, leading to a smaller temperature fluctuation. Because the evaporation rate depends exponentially on the grain temperature, photoelectron escape must be taken into consideration.

Voit (1991) considered the photoelectron escape process in the context of grain evaporation caused by absorption of X-rays from active galactic nuclei. He used a continuous approximation for energy losses suffered by an energetic photoelectron, with the losses assumed to occur continuously along the photoelectron path. This approximation is valid for energetic (larger than several hundred eV) electrons and sufficiently large grains, but it cannot be used for photoelectron energies of interest in this work, generally less than 100 eV. The energy loss in this relatively low-energy regime proceeds in a discrete manner, with a substantial fraction of the electron energy lost in single inelastic scattering events. Instead of the continuous approximation, one should consider the concept of the electron mean free path in the analysis of the photoelectron escape process. In the astrophysical context this was done by Watson (1973), who considered photoelectron escape from small dust grains with the purpose of finding how the photoelectric yield depends on the grain size. Because his purpose was to examine the efficiency of gas heating by ejected photoelectrons in the general ISM, he considered only low-energy (less than 25 eV) photons. Because at higher photoelectron energies different physical processes are important, we need to consider them in some detail.

An energetic photoelectron can undergo an elastic scattering from atomic nuclei, without any significant loss of its energy but with a change in the direction of its motion. If only elastic scatterings were important, then the photoelectron would eventually escape from the grain without losing any of its energy. Therefore, much more important are inelastic scatterings with electrons within the solid in which energy losses occur. The mean free path λ_i for the inelastic electron scattering, defined as the distance that an electron with a given energy travels between successive inelastic collisions, is the most relevant quantity determining the photoelectron escape probability. It is difficult to measure λ_i directly at the relatively low electron energies of interest here, but theoretical results for carbon are available. Tanuma, Powell, & Penn (1991) calculated the inelastic mean free paths for electrons with energies E larger than 50 eV propagating in glassy carbon. In the energy range of interest, they found λ_i to be equal to 5.9, 6.4, and 7.5 Å at 50, 100, and 150 eV, respectively. These theoretical results are in approximate agreement with experimental measurements of the electron attenuation by thin carbon films (Martin et al. 1987). The measured electron attenuation length was found to have a broad minimum at $E = 15$–200 eV, equal to 6 Å. The electron attenuation length is generally somewhat smaller than λ_i because both elastic and inelastic collisions may contribute to the attenuation. We neglect this difference in view of considerable experimental and theoretical uncertainties, and take $\lambda_i = 6$ Å in further discussion.

The probability for an electron to escape from the grain without any inelastic scattering depends not only on the inelastic mean free path but also on the initial photoelectron location and the direction of its motion. In other words, we need to know where photoelectrons are created within the grain. That requires knowledge of the electromagnetic field in the grain interior, derivable from Mie theory as done by Watson (1973). Because the mean free path for elastic scattering is comparable to the inelastic mean free path in the energy range of interest, elastic scatterings should also be taken into account. This clearly requires a separate effort; we will limit ourselves to simple estimates here. First, assume that photoelectrons are produced randomly within the grain and that their velocity distribution is isotropic. Second, neglect elastic collisions. The probability for an electron to escape from the grain without suffering an inelastic scattering is then equal to the escape probability of a photon emitted in a spherical homogeneous nebula. This probability is equal to

$$P_0(\tau) = \frac{3}{4\tau}\left[1 - \frac{1}{2\tau^2} + \left(\frac{1}{\tau} + \frac{1}{2\tau^2}\right)e^{-2\tau}\right] \tag{B1}$$

according to Osterbrock (1989), where in place of the optical radius of the nebula we use $\tau = a/\lambda_i$ (a denotes the grain radius). Escape probabilities evaluated with the help of equation (B1) are substantial for photoelectron energies and grain radii of interest. For example, we obtain $P_0 = 0.48$ for $a = 0.0007$ μm and $\lambda_i = 6$ Å.

An energetic photoelectron might still escape from the grain even after suffering an energy loss in an inelastic scattering event. This will happen if its energy after the scattering event is higher than the sum of the work function and the (positive) grain potential. The postcollision energy of an electron depends on the nature of the inelastic collision. Theoretical calculations of the inelastic mean free path by Tanuma et al. (1991) do not provide any information in this regard. In general, there is a variety of processes which can lead to an energy loss, such as an energy transfer to individual valence or core electrons, or to collective electron excitations. In our case, most important are collective excitations of valence electrons by an energetic photoelectron. These collective excitations are essentially longitudinal plasma waves modified by solid state effects. Without these effects, the electric field would oscillate with the plasma frequency $\omega_p = (4\pi n_0 e^2/m_e)^{1/2}$, where n_0 denotes the number density of electrons participating in these oscillations. The energy transferred from an electron to these waves has to be quantized, with the lowest and most probable value equal to $\hbar\omega_p$. In a

graphite grain this energy is equal to 25 eV if all four valence electrons participate in the oscillations. Because of solid state effects the actual energy in graphite is equal to 27 eV. We refer the reader to Raether (1980) for more details and references to the literature on these collective electron oscillations (plasmons) in solids. The width of a graphite plasmon at 27 eV is equal to 15 eV, a broad width caused by efficient plasmon damping within the solid. Excitations of this plasmon account for most of the energy losses of an energetic electron within a carbonaceous grain in the electron energy range from $\sim$25 to 280 eV. At higher energies excitations of core electrons also become important.

A sufficiently energetic electron is not appreciably deflected from its path when it loses its energy in a plasmon excitation. Assume, then, that photoelectrons move along straight paths even in the presence of inelastic energy losses, and neglect variations of the inelastic mean free path with electron energy. We can then simply estimate the probability of exciting exactly one plasmon by photoelectrons produced randomly within the grain. This probability P_1 is equal to $\tau_{\rm eff} \exp(-\tau_{\rm eff})$, where $\tau_{\rm eff} \equiv -\ln P_0(\tau)$, with $P_0(\tau)$ given by equation (B1). Several plasmon excitations by one photoelectron are also possible. The probability P_n of exciting exactly n plasmons is given by Poisson statistics (Raether 1980):

$$P_n = \frac{\tau_{\rm eff}^n}{n!} P_0 = \frac{\tau_{\rm eff}^n}{n!} e^{-\tau_{\rm eff}} . \tag{B2}$$

The plasmon energies are most likely to be transferred to crystal lattice oscillations, leading to an increase in grain temperature. This is the mechanism through which an energetic photon can deposit its entire energy within a small dust grain.

We account for multiple plasmon excitations in our evaporation models. Our scheme for estimating probabilities for multiple plasmon excitations and photoelectron captures should be considered as a first-order approximation to a complicated physical process. We have decided to use this scheme in our calculations because of its simplicity. While a more detailed analysis is possible, it would destroy this simplicity without a guarantee that relevant physical processes are properly accounted for. First, we assume that absorption of an energetic photon produces a photoelectron with energy $h\nu - 11.26$ eV. (The energy of 11.26 eV is the photoionization potential of atomic carbon and is meant to represent an average binding energy of valence electrons within the solid.) The distribution of photoelectrons is assumed to be uniform and isotropic within the grain. We ignore elastic scatterings and assume that inelastic collisions do not deflect photoelectrons from straight paths. The inelastic mean free path λ_i is set to 6 Å irrespective of the photoelectron energy, and the inelastic scatterings are assumed to be volume plasmon excitations with energies of 27 eV. The grain potential and its work function are assumed to be equal to 5 eV. With all these assumption it is now possible to use equations (B1) and (B2) to estimate probabilities for plasmon excitations and for the complete capture of a photoelectron. We illustrate this procedure by considering absorption of an 80 eV photon within a 0.0007 μm grain. The photoelectron energy is equal to 80–11.26 = 68.74 eV, with 11.26 eV assumed to be always deposited within the grain. With $\tau = 7/6 = 1.2$, we get $P_0 = 0.48$ from equation (B1). This is the escape probability without any plasmon excitations. The energy deposited within the grain is equal to 11.26 eV. The effective grain optical depth $\tau_{\rm eff}$ for inelastic scattering is equal to 0.73. The probability P_1 for exactly one plasmon excitation is then 0.35. The deposited energy is equal to 27 + 11.3 = 38.3 eV, with the escaping photoelectron carrying 41.7 eV. Two plasmons are excited with a probability of 0.13, with the deposited energy equal to 65.3 eV. The photoelectron with an energy of 14.7 eV can still overcome the potential barrier of 10 eV equal to the sum of the work function and the grain potential. We assume that the next inelastic scattering will lead to a capture of the photoelectron within the grain, with 80 eV deposited in the grain with a probaility of $1 - 0.48 - 0.35 - 0.13 = 0.04$. We now multiply these probabilities by the photon absorption rate calculated from Mie theory and the stellar flux intensity at the location of the grain, and insert the resulting rates in our numerical code for grain temperature fluctuations (Appendix A).

REFERENCES

Allamandola, L. J., Tielens, A. G. G. M., & Barker, J. R. 1989, ApJS, 71, 733
Balick, B. 1987, AJ, 94, 671
Barstow, M. A. 1990, MNRAS, 243, 182
Borkowski, K. J., Harrington, J. P., & Tsvetanov, Z. 1993a, ApJ, 402, L57
Borkowski, K. J., Harrington, J. P., Tsvetanov, Z., & Clegg, R. E. S. 1993b, ApJ, 415, L47
Clegg, R. E. S., Devaney, M. N., Doel, A. P., Dunlop, C. N., Major, J. V., Myers, R. M., & Sharples, R. M. 1993, in IAU Symp. 155, Planetary Nebulae, ed. R. Weinberger & A. Acker (Dordrecht: Kluwer), 388
Cohen, M., & Barlow, M. J. 1974, ApJ, 193, 401
Cohen, M., Hudson, H. S., O'Dell, S. L., & Stein, W. A. 1977, MNRAS, 181, 233
Désert, F. X., Boulanger, F., & Shore, S. N. 1986, A&A, 160, 295
Dinerstein, H. L., & Lester, D. F. 1984, ApJ, 281, 702
Gilmore, K., Koo, D., & Rank, D. 1991, in Proc. 10th Symp. on Photoelectronic Image Devices, ed. B. L. Morgan (Bristol: Inst. Physics), 113
Greenstein, J. L. 1981, ApJ, 245, 124
Guhathakurta, P., & Draine, B. T. 1989, ApJ, 345, 230
Harrington, J. P. 1986, in Proc. Workshop on Model Nebulae, ed. D. Péquignot (Paris: Observatoire de Paris), 81
Harrington, J. P., Borkowski, K. J., Blair, W. P., & Bregman, J. D. 1993, in IAU Symp. 155, Planetary Nebulae, ed. R. Weinberger & A. Acker (Dordrecht: Kluwer), 386
Harrington, J. P., Borkowski, K. J., Tsvetanov, Z., & Clegg, R. E. S. 1994, in Proc. 34th Herstmonceux Conf., Circumstellar Media in the Late Stages of Stellar Evolution, ed. R. E. S. Clegg, P. Meikle, & I. Stevens (Cambridge: Cambridge Univ. Press), in press
Harrington, J. P., Monk, D. J., & Clegg, R. E. S. 1988, MNRAS, 231, 577
Hawkins, C. W., & Zuckerman, B. 1991, ApJ, 374, 227
Hazard, C., Terlevich, B., Morton, D. C., Sargent, W. L. W., & Ferland, G. 1980, Nature, 285, 463
Heap, S. R. 1986, in New Insights in Astrophysics, ed. E. J. Rolfe (ESA SP-263), 291
Henke, B. L., Gullikson, E. M., & Davis, J. C. 1993, Atomic Data Nucl. Data Tables, 54, 181
Hora, J. L., Deutsch, L. K., Hoffmann, W. F., Fazio, G. G., & Shivanandra, K. 1993, ApJ, 413, 304
Jacoby, G. H. 1979, PASP, 91, 754
Jacoby, G. H., & Chu, Y.-H. 1989, in IAU Symp. 131, Planetary Nebulae, ed. S. Torres-Peimbert (Dordrecht: Kluwer), 183
Jacoby, G. H., & Ford, H. C. 1983, ApJ, 266, 298
Kaler, J. B., Feibelman, W. A., & Henrichs, H. F. 1988, ApJ, 324, 528
Leene, A., & Pottasch, S. R. 1988, A&A, 202, 203
Léger, A., Boissel, P., Désert, F. X., & d'Hendecourt, L. 1989, A&A, 213, 351
Lis, D. C., & Leung, C. M. 1991a, ApJ, 372, L107
———. 1991b, Icarus, 91, 7
Manchado, A., Pottasch, S. R., & Mampaso, A. 1988, A&A, 191, 128
Martin, C., Arakawa, E. T., Callcott, T. A., & Warmack, R. J. 1987, J. Electron Spectrosc. Rel. Phenom., 42, 171
Mathis, J. S., Cassinelli, J. P., van der Hucht, K. A., Prusti, T., Wesselius, P. R., & Williams, P. M. 1992, ApJ, 384, 197
Meixner, M., et al. 1993, 411, 266
Moseley, H. 1980, ApJ, 238, 892
Natta, A., Prusti, T., & Krügel, E. 1993, A&A, 275, 527
Osterbrock, D. E. 1989, Astrophysics of Gaseous Nebulae and Active Galactic Nuclei (Mill Valley: University Science Books), 385
Phillips, J. P., Sanchez Magro, C., & Martinez Roger, C. 1984, A&A, 133, 395
Pottasch, S. R., et al. 1984, A&A, 138, 10

Puget, J. L., Léger, A., & Boulanger, F. 1985, A&A, 142, L19
Raether, H. 1980, Excitations of Plasmons and Interband Transitions by Electrons (New York: Springer-Verlag)
Reay, N. K., Atherton, P. D., & Taylor, K. 1983, MNRAS, 203, 1079
Robertson, J. 1986, Adv. Phys., 35, 317
Rouleau, F., & Martin, P. G. 1991, ApJ, 377, 526
Siebenmorgen, R., & Krügel, E. 1992, A&A, 259, 614
Siebenmorgen, R., Krügel, E., & Mathis, J. S. 1992, A&A, 266, 501
Tanuma, S., Powell, C. J., & Penn, D. R. 1991, Surf. Interface Anal., 17, 911
Todorovic, P. 1992, An Introduction to Stochastic Processes and Their Applications (New York: Springer-Verlag), 81
Voit, G. M. 1991, ApJ, 379, 122
———. 1992, MNRAS, 258, 841
Watson, W. D. 1973, J. Opt. Soc. Am., 63, 164
Werner, K., & Koesterke, L. 1992, in The Atmospheres of Early-Type Stars, ed. U. Heber & C. S. Jeffery (Berlin: Springer-Verlag), 288
Willner, S. P., Becklin, E. E., & Visvanathan, N. 1972, ApJ, 175, 699
Wright, E. L. 1993, in AIP Conf. Proc. 278, Back to the Galaxy, ed. S. S. Holt & F. Verter (New York: AIP), 193
Yadoumaru, Y., & Tamura, S. 1994, PASP, 106, 165
Zhang, C. Y., & Kwok, S. 1992, ApJ, 385, 255